Controlling hollow relativistic electron beam orbits with an inductive current divider

S. B. Swanekamp (ID), A. S. Richardson, J. R. Angus, G. Cooperstein, D. D. Hinshelwood, P. F. Ottinger (ID), I. M. Rittersdorf, J. W. Schumer, B. V. Weber, and J. C. Zier

View Online   Export Citation   CrossMark

ARTICLES YOU MAY BE INTERESTED IN

Controlling hollow relativistic electron beam orbits with an inductive current divider

S. B. Swanekamp, A. S. Richardson, J. R. Angus, G. Cooperstein,[a] D. D. Hinshelwood, P. F. Ottinger,[a] I. M. Rittersdorf,[b] J. W. Schumer, B. V. Weber, and J. C. Zier

Plasma Physics Division, Naval Research Laboratory, Washington, DC 20375, USA

A passive method for controlling the trajectory of an intense, hollow electron beam is proposed using a vacuum structure that inductively splits the beam's return current. A central post carries a portion of the return current (I_1), while the outer conductor carries the remainder (I_2). An envelope equation appropriate for a hollow electron beam is derived and applied to the current divider. The force on the beam trajectory is shown to be proportional to (I_2-I_1), while the average force on the envelope (the beam width) is proportional to the beam current $I_b = (I_2 + I_1)$. The values of I_1 and I_2 depend on the inductances in the return-current path geometries. Proper choice of the return-current geometries determines these inductances and offers control over the beam trajectory. Solutions using realistic beam parameters show that, for appropriate choices of the return-current-path geometry, the inductive current divider can produce a beam that is both pinched and straightened so that it approaches a target at near-normal incidence with a beam diameter that is on the order of a few mm. © 2015 AIP Publishing LLC. [http://dx.doi.org/10.1063/1.4907663]

I. INTRODUCTION

External control of the electron orbits for an intense electron beam is useful for many applications. For applications where the goal is to maximize the x-ray dose in the forward direction, the ability to control the electron incident angle with the x-ray target is advantageous since the bremsstrahlung emission is peaked in the direction of the electron orbit. Such is the case for Intense Pulsed Active Detection[1] (IPAD) where an intense bremsstrahlung source is used to actively induce fissions for active interrogation of fissile material at large stand-off distances. For flash radiography, it is beneficial to focus the intense beam to as small of a diameter as possible while maintaining relatively small angles with the converter.[2] Having external control over the beam is important for these and other applications where both beam size and angle are essential.

Hollow, annular electron beams are easily created with modern pulsed-power architectures such as an inductive voltage adder[3] or linear transformer device[4] that rely on magnetic insulation to confine electron flow to a central cathode stalk along which the voltage is added in stages that are inductively isolated. Both the generation and control of the beam angle at the end of a magnetically insulated transmission line (MITL) have been studied previously using an annular electron beam with an indented-anode geometry.[5,6] However, the indented-anode geometry offers limited control over the beam's radius and angle. More control over these parameters is possible by manipulating the beam orbits external to the accelerator.

There are examples in the literature where an annular beam is extracted from an accelerator and controlled externally by using actively produced plasmas and/or by applying external magnetic fields produced from an external power source. One example of this is the compound lens where a hollow electron beam is extracted from an accelerator into a cavity containing N_2 gas.[7] The gas facilitates rapid charge and current neutralization of the incident beam. Beam control in the compound lens is achieved by a magnetic field produced by boundary currents powered by an external power supply.

In the present paper, a totally passive method is proposed that uses the return currents of the beam to achieve similar results. This method has the advantage over active techniques in that no external plasma or power sources are required. The beam is extracted through a range-thin foil into a cylindrical vacuum cavity as shown in Fig. 1. The cavity acts as an inductive-current divider where a portion of the beam's return current, I_1, flows through a central post of radius R_0 and the remainder, I_2, flows through the outer conductor with radius R_w.

Applying Faraday's law to the cavity shows that the magnetic flux must remain constant during the beam pulse because there is a closed path entirely inside a conductor where $\oint E \cdot d\ell = 0$. In the present analysis, the magnetic flux is assumed to be initially zero. Therefore, it must remain zero throughout the beam pulse as well. This means that the beam must take a path where the magnetic flux associated with the two return currents remain equal and opposite. In this case, flux balance can be written as

$$L_1 I_1 = L_2 I_2, \qquad (1)$$

where L_1 is the inductance associated with the return current, I_1, that flows in the central post and L_2 is the inductance associated with the current, I_2, that flows in the outer wall. In this paper, currents and current density are expressed as positive quantities, while other quantities such as the electric and

---
[a]Independent consultant through Engility Corp.
[b]Postdoctoral research associate with the National Research Council at the Naval Research Laboratory.
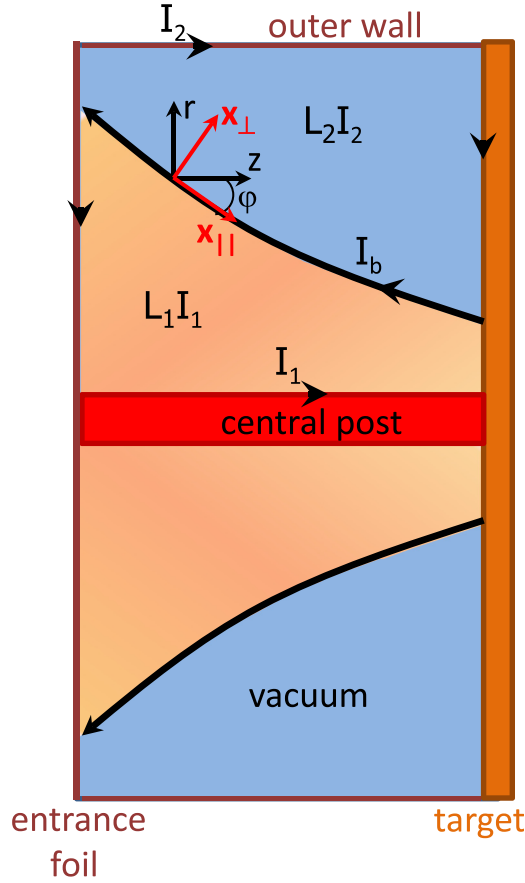
FIG. 1. A schematic of the inductive-current divider.

magnetic fields retain their proper sign. The beam current is the sum of the two return currents ($I_b = I_1 + I_2$) and Eq. (1) becomes

$$L_2 I_2 = \left(\frac{L_1 L_2}{L_1 + L_2} \right) I_b,$$

$$(I_2 - I_1) = \left(\frac{L_1 - L_2}{L_1 + L_2} \right) I_b, \qquad (2)$$

where the inductances depend on the path taken by the beam. The inductances in the above equation are given by

$$L_{1,2} = \frac{1}{I_{1,2}} \iint\limits_{A_{1,2}} B_\theta \, dA, \qquad (3)$$

where the integrations are performed over the areas $A_{1,2}$ that are below (L_1) and above (L_2) the path of the beam. Equation (2) shows that the beam current is inductively split and that, when $L_1 \gg L_2$ nearly the entire beam current returns through the outer wall. In the opposite limit, nearly all the beam current returns through the central post. Therefore, the values of I_1 and I_2 are controlled by changing the relative values of the inductances in the return-current paths. Even though Fig. 1 shows a fairly simple return-current-path geometry, Eqs. (1)–(3) hold for more complex return-current paths.

An analysis of the current-divider using the beam envelope equation and its application to either straighten or focus the beam is presented in the remainder of the paper. Except where

explicitly stated, cgs units are used in the analysis. A breakdown of the electric and magnetic forces on a thin, annular beam is presented in Sec. II. The envelope equations appropriate for a finite thickness, annular beam are presented in Sec. III. Section IV presents solutions to the hollow-beam envelope equations for two important cases using realistic beam parameters. The first solution shows that, with appropriate choice of the return-current geometry, the beam trajectory can be straightened so that it approaches a target at normal incidence. The second solution shows the possibility of obtaining a very tightly pinched beam with a beam diameter of a few mm and a trajectory that is close-to-normal at the target. Important conclusions of the paper and future work are presented in Sec. V.

II. FORCES ON A THIN ANNULAR BEAM

In this section, the electric and magnetic forces on a thin, annular beam are analyzed. A thin, annular beam is one where the average beam radius is large compared to the width so that fluctuations in the beam envelope can be ignored. The transverse force on the beam is

$$F_\perp = -e(E_\perp - \beta_0 B_\theta) = F_E + F_B, \qquad (4)$$

where e is the magnitude of the electron charge, $E_\perp$ is the electric field perpendicular to the beam trajectory produced by its own space charge, B_θ is the self-magnetic field produced by the beam current, β_0 is the beam velocity parallel to the orbit normalized by the speed of light, and $F_E = -eE_\perp$ and $F_B = e\beta_0 B_\theta$ are the electric and magnetic forces.

Averages in the transverse direction are used in much of the following analysis. In general, the transverse average of any quantity, G, can be defined as

$$\langle G \rangle = \frac{1}{I_b} \int\limits_{-\infty}^{\infty} G(x_\perp) J_b(x_\perp) 2\pi r(x_\perp) dx_\perp, \qquad (5)$$

where $\langle \, \rangle$ is used to denote the transverse average, $x_\perp$ is a coordinate perpendicular to both the beam trajectory and the magnetic field (see Fig. 1), and J_b is the beam current density. In Eq. (5), the quantity $2\pi r J_b dx_\perp$ is the beam current between $x_\perp$ and $x_\perp + dx_\perp$ so that $2\pi r J_b / I_b$ is a probability density. In the thin-beam limit, the probability density function is $2\pi r J_b / I_b = \delta(r - r_b)$, where r_b is the radius of the thin annular beam. The analysis is considerably simplified in this limit.

The electric field in the current divider can be derived by solving

$$\nabla^2 \Phi = 0 \qquad (6)$$

in the two regions where displacement currents have been ignored. Region 1 is associated with the return-current path through the central post, while region 2 is associated with the return-current path through the outer wall. The boundary conditions are $\Phi = 0$ on the conducting boundaries and $\Phi = \Phi_b(s)$ along the beam path, where $s = c\beta_0 t$ is the coordinate along the beam path. In addition to these boundary conditions, the jump condition for the electric field is given by

$r_b E_\perp^+ - r_b E_\perp^- = -\lambda_b$, where $\lambda_b = I_b/(c\beta_0)$ is the magnitude of the beam's linear charge density, and $E_\perp^\pm$ is the perpendicular electric field component just outside (+) and inside (-) the beam orbit. An analytic solution to Eq. (6) is difficult. However, useful information can be obtained by multiplying Eq. (6) by Φ and integrating over the volume of each region. After integrating by parts and applying the divergence theorem, the following integral relation is obtained:

$$\pm \frac{1}{2} \int_0^{s_0} ds \Phi_b r_b E_\perp^\pm = \int d^3x \frac{\mathbf{E}_{1,2}^2}{4\pi}, \qquad (7)$$

where the lower (upper) sign corresponds to the component just inside (outside) the beam, and $\mathbf{E}_{1(2)}$ is the total electric field vector resulting from these charges in region 1 (2). The source of the electric field in each region is the beam space charge and the positive surface charges induced by the beam on the conducting surfaces. Applying the jump condition yields

$$-\frac{1}{2} \int_0^{s_0} ds \Phi_b \lambda_b = \int d^3x \frac{\mathbf{E}_1^2 + \mathbf{E}_2^2}{8\pi}. \qquad (8)$$

The left hand side of this equation is the work done by the beam. This work goes into creating the electric fields inside the current divider and is equal to the total electrostatic energy.

The potential, Φ_b, is negative along the beam path and arises from the beam's space charge and the positive image charges induced on the conducting surfaces. As the beam leaves the entrance foil, the magnitude of Φ_b increases creating primarily an electric field parallel to the beam trajectory. This field is caused by positive image charges induced on entrance foil, which produces an attractive force on the beam electrons. This pull on the beam causes it to slow down and lose energy. As the beam moves more than a few times the radial gap, (R_w-R_0), away from the entrance foil, the parallel electric field decreases rapidly and Φ_b changes more slowly. In this region, the electric field is mainly transverse to the beam trajectory. As the beam approaches the target, it is now attracted to the positive image charges induced there and it gains energy. In this region, the magnitude of Φ_b decreases rapidly to zero and the beam gains back all the energy it lost as it entered the current divider. Therefore, the beam strikes the target with the same kinetic energy it had as it entered the current divider.

There is a limit to the amount of current that can be injected into the vacuum current divider. At this limit, the potential depression created by the beam's space charge is deep enough to reflect a portion of the beam forming a virtual cathode. An estimate of the space-charge-limited current for a hollow beam in an infinitely-long, hollow tube is[8]

$$I_{SCL} = I_A \frac{\left(\gamma_0^{2/3} - 1\right)^{3/2}}{2\ln(R_w/r_b)}, \qquad (9)$$

where $(\gamma_0 - 1)mc^2$ is the beam's kinetic energy, $I_A = (mc^3/e)$ = 17 kA, m is the electron rest mass, and c is the speed of light. Although strictly valid when the cavity length, ℓ, is large compared to beam radius, this expression is within

10% of the true value when $\ell/r_b \sim 1$. When no ions are present, the injected beam current into the current divider should be well below the space-charge-limiting current. This is because loss of radial confinement of the beam can occur if the beam energy drops too low. This loss occurs because the confining magnetic force decreases with the beam energy allowing the strong repulsive electric field to dominate. However, if positive space charge is present to neutralize the beam's space charge, the injected beam current can be substantially larger than I_{SCL}. This can happen, for example, if the specific energy deposition by the beam in the target is large enough to create plasma.

In the thin-beam limit, the transverse electric field experienced by the beam is the average of the field on either side of the jump. In this case,

$$\langle E_\perp \rangle = \frac{1}{2}\left(E_\perp^+ + E_\perp^-\right). \qquad (10)$$

If

$$\overline{\langle r_b E_\perp \rangle} \equiv \int_0^{s_0} ds \Phi_b \langle r_b E_\perp \rangle \bigg/ \int_0^{s_0} ds \Phi_b \qquad (11)$$

is defined to be the potential-weighted, path-length average of $\langle r_b E_\perp \rangle$, then it is possible to write

$$\overline{\langle r_b E_\perp \rangle} = \lambda_b \frac{\int d^3x \left(\mathbf{E}_1^2 - \mathbf{E}_2^2\right)}{\int d^3x \left(\mathbf{E}_1^2 + \mathbf{E}_2^2\right)}. \qquad (12)$$

Equation (12) shows that the path-length-averaged transverse electric field is proportional to the difference of the electric field energies in each region.

The capacitance per unit length in each region can be defined by

$$\int_0^{s_0} \frac{1}{2} C_{1,2} \Phi_b^2 ds \equiv \int \frac{E_{1,2}^2}{4\pi} d^3x. \qquad (13)$$

With these definitions, $\overline{\langle r_b E_\perp \rangle}$ becomes

$$\overline{\langle r_b E_\perp \rangle} = \lambda_b \frac{\int (C_1 - C_2)\Phi_b^2 ds}{\int (C_1 + C_2)\Phi_b^2 ds}. \qquad (14)$$

This equation shows that the sign of the perpendicular electric field depends on the capacitances in the two return-current geometries. When $C_1 > C_2$, the perpendicular electric field is positive and the perpendicular electric force is negative. Furthermore, when $C_1 = C_2$ the transverse electric field is zero and the electric force is zero. This is in contrast to an electron beam in free space where the electric force is always positive.

In the long-beam limit defined by $\ell/(R_w$-$R_0) \gg 1$, end effects can be ignored and Φ_b, C_1, and C_2 vary slowly along s. In this limit, we can write

$$\langle E_\perp \rangle = \frac{\lambda_b}{r_b} \frac{(C_1 - C_2)}{(C_1 + C_2)}. \qquad (15)$$

Since the capacitance and inductance per unit length are related by $C_{1,2} = c^2/L_{1,2}$, there is a simple relationship between $E_\perp$ and B_θ in the long-beam limit. This relationship can be written as

$$\langle E_\perp \rangle = \frac{I_b}{r_b c \beta_0} \frac{(L_2 - L_1)}{(L_2 + L_1)} = \frac{\langle B_\theta \rangle}{\beta_0}, \qquad (16)$$

where (see Eq. (22) below)

$$\langle B_\theta \rangle = \frac{I_b}{r_b c} \frac{(L_2 - L_1)}{(L_2 + L_1)}. \qquad (17)$$

Substituting Eq. (16) into Eq. (4) gives

$$\langle F_\perp \rangle = \langle F_E \rangle / \gamma_0^2 = -\langle F_B \rangle / (\gamma_0^2 \beta_0^2). \qquad (18)$$

This shows that, similar to a beam in free space, the transverse electric and magnetic forces on the beam cancel each other to order $1/\gamma_0^2$ in the long-beam limit.[9] In contrast to a beam in free space, the direction of the average force depends on the return-current geometry.

For the inductive current divider, there are two potential sources of positive charge that reduce the transverse electric field specified in Eq. (16). These two sources depend on the specific energy deposited by the beam in the target and the ratio $\ell/(R_w-R_0)$. For low deposited energies, the main source of field reduction comes from positive surface charges on the entrance foil and beam target. These surface charges produce primarily a parallel electric field and can "short out" the transverse electric field. Therefore, when the gap between the entrance foil and the beam target is comparable to or smaller (R_w-R_0), the transverse electric field is significantly smaller than the value given by Eq. (16). A similar phenomenon has been investigated for thin-foil focusing of solid beams.[10,11] In that work, it was found that a significant reduction of the transverse electric field occurs when the gap between the thin foils and the outer wall radius is comparable (i.e., $\ell \sim R_w$). When $\ell = R_w$, it was shown that the transverse electric field averaged over the beam path is reduced by a factor between 0.4 and 0.8 depending on the value of r_b/R_w.

When the beam current density at the target is sufficiently large, the specific energy deposition can be large enough to produce surface plasma from outgassing.[12] In this case, the main source of electric field reduction is from the flow of positive space charge from this plasma back along the beam trajectory. The ion current from this plasma is typically small compared to the electron current and its effect on the magnetic field is negligible. However, this flow of ions can result in significant space-charge neutralization along the entire length of the electron beam. In this case, the magnitudes of both the parallel and transverse electric fields are reduced and the injected beam current can exceed the vacuum space-charge-limited current.

If f_i is the factor by which the transverse electric field is reduced by either surface and/or space charges, then Eq. (16) can be rewritten as

$$\langle E_\perp \rangle = (1 - f_i) \frac{\langle B_\theta \rangle}{\beta_0}. \qquad (19)$$

It should be noted that, in the case where the reduction is due to surface charges, f_i is the path-averaged reduction. This simplification neglects the variation of the electric field along the beam path. With these assumptions, the transverse force on the beam can be rewritten as

$$\langle F_\perp \rangle = \frac{(f_i - 1/\gamma_0^2)}{\beta_0^2} \langle F_B \rangle, \qquad (20)$$

where $\langle F_B \rangle = e\beta_0 \langle B_\theta \rangle$ is the transverse-averaged magnetic force. This equation shows that, when $f_i > 1/\gamma_0^2$, the net transverse force is in the same direction as the magnetic force.

The magnetic field in the current divider can be written as

$$cB_\theta = \begin{cases} \dfrac{2I_1}{r} & R_0 \leq r < r_b \\[2mm] -\dfrac{2I_2}{r} & r_b < r \leq R_w. \end{cases} \qquad (21)$$

The transverse average of the magnetic field is given by the average magnetic field on either side of the jump. The result is

$$\langle cB_\theta \rangle = -\frac{(I_2 - I_1)}{r_b} = \frac{I_b}{r_b} \frac{(L_2 - L_1)}{(L_2 + L_1)}. \qquad (22)$$

Substituting Eq. (22) into Eq. (20) gives the following important result:

$$\frac{\langle F_\perp \rangle}{\gamma_0 mc^2 \beta_0^2} = \frac{(f_i - 1/\gamma_0^2)}{\gamma_0 \beta_0^3} \left(\frac{I_b}{I_A r_b} \right) \frac{(L_2 - L_1)}{(L_2 + L_1)}. \qquad (23)$$

This equation shows that the normalized transverse force on the beam is proportional to $(L_2 - L_1)$ and varies as $1/r_b$. Moreover, when $L_1 > L_2$ the net force is negative and when $L_1 < L_2$ the force is positive. When $L_1 = L_2$, the two return currents are equal, the average transverse force on the beam is zero, and the beam trajectory is ballistic.

Equations of motion for the thin annular beam come from

$$\boldsymbol{p} = p_0 \hat{e}_\|, \qquad (24)$$

where $p_0 = \gamma_0 mc\beta_0$ is the directed momentum of the beam and $\hat{e}_\|$ is the unit vector parallel to the beam trajectory. Differentiating Eq. (24) with respect to time gives

$$\frac{d\boldsymbol{p}}{dt} = \frac{dp_0}{dt} \hat{e}_\| + p_0 \dot{\varphi} \hat{e}_\perp = \boldsymbol{F}, \qquad (25)$$

where φ is the angle between the beam trajectory and the z-axis, and $\hat{e}_\perp = \dot{\varphi} \hat{e}_\|$ is the unit vector perpendicular to the beam trajectory (see Fig. 1). Using the relation $d\gamma_0/dt = \beta_0 \gamma_0^3 (d\beta_0/dt)$ allows the acceleration parallel to the beam trajectory to be expressed as

$$\frac{d(c\beta_0)}{dt} = \frac{\langle F_\| \rangle}{\gamma_0^3 m}, \qquad (26)$$

where $\langle F_\| \rangle$ is the transverse-averaged force parallel to the beam trajectory. For a relativistic beam with $\gamma_0 \gg 1$, the parallel acceleration is small and can be ignored. In this limit,

the beam's directed energy remains constant and the perpendicular force simply acts to change the beam's direction. This approximation is valid provided either that the beam current is significantly below the space-charge limit or that a significant ion charge is present to neutralize the beam charge. The equation of motion perpendicular to the beam can now be written as

$$\frac{d\phi}{ds} = \frac{\langle F_\perp \rangle}{\gamma_0 mc^2 \beta_0^2}, \tag{27a}$$

$$\frac{dr_b}{ds} = \sin(\varphi),$$

$$\frac{dz_b}{ds} = \cos(\varphi), \tag{27b}$$

where $ds = c\beta_0 dt$ is the increment in beam's path length and $\mathbf{r_0} = (r_b, z_b)$ is the vector that traces out the path followed by the thin annular beam. In Eq. (27), the sign of the angle φ is negative when the beam is focused radially inward.

In principle, Eqs. (3), (23), and (27) can be solved iteratively for a specified geometry. In practice, a given beam condition is usually required at the beam target. In this situation, it is easier to vary the return-current difference in Eq. (22) until this beam condition is achieved. A return-current geometry that provides the inductance ratio consistent with this beam path is then determined from Eq. (3) using the required beam path.

III. ENVELOPE ANALYSIS

A. The envelope equation for an annular beam

In some applications, the variation of the beam width along the beam trajectory is also important. In this case, an envelope analysis can be performed. The three main assumptions made in the derivation of an envelope equation are: (1) The transverse energy spread is small compared to the directed beam energy (the paraxial assumption), (2) gradients along the beam path are small compared to gradients perpendicular to the beam, and (3) the beam current density, the electric field, and the magnetic field are all azimuthally symmetric.

The goal in this section is to derive a differential equation for X_b, the root-mean-squared (rms) deviation from the average beam orbit in a direction perpendicular to the average beam orbit. The mean square deviation is defined by $X_b^2 = \langle |\mathbf{r} - \mathbf{r_0}|^2 \rangle$, where $\mathbf{r} = (r, z)$ is a typical beam-particle orbit, $\mathbf{r_0} = (r_b, z_b)$ is the average beam orbit, and now $\langle \ \rangle$ represents the transverse phasespace average defined below. The beam orbits can be written as $\mathbf{r} = \mathbf{r_0} + x_\perp \hat{e}_\perp$, where $\hat{e}_\perp$ is the unit vector perpendicular to the beam path and $x_\perp$ is the position of the beam particle along that direction. The parallel component is ignored because it is small in the paraxial limit. In this case, the mean-square deviation from the average orbit can be written as

$$X_b^2 = \langle x_\perp^2 \rangle. \tag{28}$$

The meaning of X_b can be obtained from Chebyshev's theorem that states a minimum of 75% of the samples from a random variable lie within two standard deviations of the mean independent of the underlying probability distribution.[13,14] Therefore, the curves traced out by $\mathbf{r}^\pm = \mathbf{r_0} \pm 2X_b \hat{e}_\perp$ contain at least 75% of the beam particles. In practice, common transverse probability distributions assumed for the beam contain significantly more than 75% of the beam particles. It is not surprising that the curves traced out by $\mathbf{r}^\pm$ are called the beam envelope.

The envelope equation for an annular beam is derived following an approach similar to that used in Ref. 15 for a sheet beam. The phasespace distribution function, f_b, can be obtained from a solution of the Vlasov-Maxwell equations. For a general coordinate system, the Vlasov equation can be written as

$$\frac{\partial f_b}{\partial t} + \{f_b, \mathscr{H}\} = 0, \tag{29}$$

where $\mathscr{H}$ is the single-particle Hamiltonian in that coordinate system. The bracket notation used in Eq. (29) represents the Poisson bracket defined by

$$\{f_b, \mathscr{H}\} \equiv \frac{\partial f_b}{\partial q} \cdot \frac{\partial \mathscr{H}}{\partial P} - \frac{\partial f_b}{\partial P} \cdot \frac{\partial \mathscr{H}}{\partial q}, \tag{30}$$

where q and P are the canonical coordinates for the chosen coordinate system.

The Hamiltonian that describes a hollow beam in a coordinate system perpendicular to the beam path can be written as

$$\mathscr{H} = \left[\left(P_0 + \frac{e}{c} A_0(x_\perp) \right)^2 c^2 + m^2 c^4 \right]^{1/2} + \frac{p_\perp^2}{2\gamma_0 m} - e\Phi(x_\perp), \tag{31}$$

where $P_0 = p_0 - eA_0/c$ is the canonical momentum parallel to the beam trajectory, $p_0 = \gamma_0 mc\beta_0$ is the beam's directed momentum, $\Phi(x_\perp)$ is the electric potential, $A_0(x_\perp)$ is the magnetic vector potential, and $p_0 \gg p_\perp$ has been assumed. In this coordinate system, the parallel canonical momentum, P_0, is a constant of the motion and the perpendicular canonical coordinates are $q_\perp = x_\perp$ and $P_\perp = p_\perp$, which satisfy Hamilton's equations

$$\dot{x}_\perp = \frac{\partial \mathscr{H}}{\partial p_\perp} = \frac{p_\perp}{\gamma_0 m},$$

$$\dot{p}_\perp = -\frac{\partial \mathscr{H}}{\partial x_\perp} = F_\perp. \tag{32}$$

The phasespace average of a general function of phasespace variables, $g(x_\perp, p_\perp)$, is defined as

$$\langle g \rangle = \frac{ec\beta_0}{I_b} \int \int 2\pi r \, dx_\perp dp_\perp \, g f_b, \tag{33}$$

where the transverse electron phasespace-distribution function, $f_b(x_\perp, p_\perp, t)$, is normalized so that the integral over $p_\perp$ gives the beam density $n_b = J_b/(ec\beta_0)$. The transverse phasespace average defined in Eq. (33) is identical to that given by Eq. (5) provided that $G(x_\perp)$ is the $p_\perp$ moment of g. By taking the derivative of Eq. (33) with respect to the path length,

$s = c\beta_0 t$, using Eq. (29) to eliminate $\partial f_b/\partial s$, and integrating by parts, it is possible to express the rate of change of $\langle g \rangle$ along s as

$$\frac{d\langle g \rangle}{ds} = \frac{1}{c\beta_0}\langle\{g, \mathcal{H}\}\rangle,$$
$$= \frac{1}{c\beta_0}\left\langle \frac{p_\perp}{\gamma_0 m}\frac{\partial g}{\partial x_\perp} + F_\perp \frac{\partial g}{\partial p_\perp}\right\rangle. \quad (34)$$

In the second form of the above equation, the Poisson bracket has been expanded and Hamilton's equations (Eq. (32)) have been used to eliminate $\mathcal{H}$.

While it is possible to derive the envelope equation by ensemble averages over the single-particle equations of motion as done in Ref. 9, the derivation is greatly simplified by repeated application of Eq. (34) with appropriate choices for g. In addition, by using Eq. (34) the derivation explicitly shows the connection of the envelope equation to the Vlasov equation.

The equations of motion for the beam can be derived using $g = x_\perp$ and $g = p_\perp$ in Eq. (34). These equations are given by

$$\frac{d\langle x_\perp \rangle}{ds} = \frac{\langle p_\perp \rangle}{p_0}, \quad (35a)$$

$$\frac{d\langle p_\perp \rangle/p_0}{ds} = \frac{\langle F_\perp \rangle}{\gamma_0 mc^2 \beta_0^2}. \quad (35b)$$

Since $d\langle p_\perp \rangle/p_0 \equiv d\varphi$, Eq. (35b) is equivalent to the equation of motion for a thin annular beam given by Eq. (27a). The difference here is that now $\langle F_\perp \rangle$ is calculated from a beam current density that is no longer a δ-function in space.

By application of the chain rule to Eq. (28), an intermediate equation for the rms deviation from the average orbit can be written as

$$\frac{dX_b}{ds} = \frac{1}{2X_b}\frac{d\langle x_\perp^2 \rangle}{ds}. \quad (36)$$

Using $g = x_\perp^2$ and $g = x_\perp p_\perp$ in Eq. (34), the following other useful intermediate quantities are obtained:

$$\frac{d\langle x_\perp^2 \rangle}{ds} = 2\frac{\langle x_\perp p_\perp \rangle}{p_0},$$
$$\frac{d\langle x_\perp p_\perp \rangle}{ds} = p_0\left(\frac{\langle p_\perp^2 \rangle}{p_0^2} + \frac{\langle x_\perp F_\perp \rangle}{\gamma_0 mc^2 \beta_0^2}\right). \quad (37)$$

The desired equation for the rms deviation of the beam is obtained by combining Eqs. (36) and (37). This equation is given by

$$\frac{d^2 X_b}{ds^2} = \frac{\langle x_\perp F_\perp \rangle/(\gamma_0 mc^2 \beta_0^2)}{X_b} + \frac{\varepsilon^2}{X_b^3}, \quad (38)$$

where

$$\varepsilon^2 = \frac{\langle p_\perp^2 \rangle\langle x_\perp^2 \rangle}{p_0^2} - \left(X_b \frac{dX_b}{ds}\right)^2$$
$$= \frac{\langle p_\perp^2 \rangle\langle x_\perp^2 \rangle - \langle x_\perp p_\perp \rangle^2}{p_0^2} \quad (39)$$

is the unnormalized beam emittance and

$$\frac{\langle x_\perp F_\perp \rangle}{X_b \gamma_0 mc^2 \beta_0^2} \equiv \left(\frac{(f_i - 1/\gamma_0^2)}{\gamma_0 \beta_0^3 I_A r_b}\right)\frac{\langle x_\perp cB_\theta \rangle}{X_b} \quad (40)$$

is the normalized average self-force on the rms envelope. This equation indicates that the average self-force on the envelope is proportional to average torque on the beam. This torque, in turn, is proportional to the centroid of the magnetic field.

The emittance is the transverse-phasespace area occupied by the beam. In many situations, the emittance does not change along the beam path and can be taken to be constant. However, one important exception that can cause significant changes in ε is the presence of strong self-fields.[15] An equation for the change of ε with s can be derived by differentiating Eq. (39) and applying Eq. (34) to the result. This equation can be written as

$$\frac{d\varepsilon}{ds} = \frac{X_b}{\varepsilon}\left(\frac{\dfrac{X_b\langle p_\perp F_\perp \rangle}{p_0} - \dfrac{dX_b}{ds}\langle x_\perp F_\perp \rangle}{\gamma_0 mc^2 \beta_0^2}\right). \quad (41)$$

This equation shows the prominent role that the beam's self-force plays in emittance growth. In the envelope analysis given below, changes in the emittance are assumed to be small compared to the initial emittance of the beam.

The equation of motion for the average orbit (Eq. (35)) and beam envelope equation (Eq. (38)) are direct consequences of the Vlasov Equation. As pointed out in Ref. 15, these equations do not form a closed dynamical system since they depend on the current density through the quantities $\langle F_\perp \rangle$ and $\langle x_\perp F_\perp \rangle$. An exact, self-consistent expression for J_b can only be determined from a full solution of the non-linear Vlasov-Maxwell equations. However, valuable scaling information can be obtained using an approximate form for J_b without needing detailed knowledge of the underlying phase-space distribution.

B. The average force and torque for a uniform-current distribution

As an example of the application of the envelope equations, consider a beam current density given by

$$J_b(r_b, x_\perp) = \begin{cases} \dfrac{I_b}{2\pi(r_b + x_\perp \cos\varphi)w} & |x_\perp| < \dfrac{w}{2} \\ 0 & \text{otherwise,} \end{cases} \quad (42)$$

where w is the width of the beam. Changes in the current density as the beam propagates are assumed to occur self-similarly through changes of w, r_b, and φ along the beam path, s. With this choice, $2\pi r J_b$ is independent of $x_\perp$ and the beam current is distributed uniformly in the direction perpendicular to $\mathbf{r_0}$. The rms deviation is related to the beam width by

$$X_b = \left(\frac{1}{I_b}\int_{-\infty}^{\infty} x_\perp^2 2\pi\, rJ_b dx_\perp\right)^{1/2} = \frac{w}{\sqrt{12}},$$

for this current density distribution and the envelope defined by $\mathbf{r}^{\pm} = \mathbf{r_0} \pm 2X_b \hat{e}_{\perp}$ contains 100% of the beam orbits.

With the form of J_b given by Eq. (42), the magnetic field can be determined from Ampere's law and written as

$$
cB_\theta = \frac{2}{(r_b + x_\perp \cos\varphi)}
\begin{cases}
I_1 & x_\perp < -\dfrac{w}{2} \\[6pt]
I_1 - I_b(x_\perp/w + 1/2) & |x_\perp| < \dfrac{w}{2} \\[6pt]
-I_2 & x_\perp > \dfrac{w}{2}
\end{cases}.
$$

(43)

From this expression, the transverse average of the magnetic field can be expressed as

$$
\langle cB_\theta \rangle = -\frac{I_b}{r_b}\left\{ \frac{(I_2 - I_1)}{I_b}\frac{1}{\xi_w}\ln\left(\frac{1 + \xi_w/2}{1 - \xi_w/2}\right) \right.
$$
$$
\left. -\frac{2}{\xi_w^2}\left[\ln\left(\frac{1 + \xi_w/2}{1 - \xi_w/2}\right) - \xi_w\right]\right\}
$$
$$
\cong -\frac{I_b}{r_b}\left[\frac{(I_2 - I_1)}{I_b}\left(1 + \frac{\xi_w^2}{12}\right) - \frac{\xi_w}{6}\right],
$$

(44)

where $\xi_w \equiv w\cos(\varphi)/r_b$ is the normalized beam width. It is important to note that Eq. (44) approaches the thin-beam limit when $w/r_b \to 0$. This is seen in the last form of Eq. (44), which is the result of a Taylor-series expansion about $\xi_w = 0$. Surprisingly, this expansion remains within 5% of the true value even for values of ξ_w as large as 1.3.

A plot of the normalized average magnetic field as a function of the normalized width for several values of $(I_2–I_1)/I_b$ is shown in Fig. 2. From this plot, it is evident that the solution diverges as $\xi_w \to 2$ because, in this limit, the inner envelope approaches $r = 0$. In this case, the assumption of a hollow beam is no longer valid. A special case occurs when $I_2 = I_b$ and $I_1 = 0$ so that $(I_2-I_1)/I_b = 1$. For this special

case, the magnetic field between the central post and the beam's inner envelope is zero and the average magnetic field remains finite as $\xi_w \to 2$. In practice, the presence of the central post prevents the beam envelope from ever reaching $r = 0$. This plot further shows that there is no value of $(I_2-I_1)/I_b$ that makes the beam force-free for all values of ξ_w. The best choice for minimizing the transverse force is to choose $(I_2-I_1)/I_b$ slightly larger than 0.0 so that the path-length-averaged force on the beam remains small as the beam propagates and its envelope oscillates about its force-free equilibrium.

For the current density specified in Eq. (42), the magnetic-field centroid is computed in a similar fashion to that used to arrive at Eq. (44). This normalized magnetic-field centroid can be expressed as

$$
\frac{\langle x_\perp cB_\theta \rangle}{X_b} = -\frac{wI_b}{X_b r_b}\left\{ \frac{2}{\xi_w^3}\left[\ln\left(\frac{1 + \xi_w/2}{1 - \xi_w/2}\right) - \xi_w\right]\right\}
$$
$$
\times \left(1 - \frac{(I_2 - I_1)}{2I_b}\xi_w\right)
$$
$$
\cong -\frac{I_b}{r_b}\frac{2\sqrt{3}}{3}\left(1 - \frac{(I_2 - I_1)}{2I_b}\xi_w\right) \times \left(1 + 0.2\xi_w^2\right).
$$

(45)

The last term again is obtained from a Taylor-series expansion about $\xi_w = 0$, which is accurate to within 5% for $\xi_w \le 1.3$.

A plot of the normalized magnetic field centroid as a function of ξ_w is given in Fig. 3 for several values of $(I_2-I_1)/I_b$. The centroid of the magnetic field is negative because B_θ varies as $1/r$ and therefore is larger for negative values of $x_\perp$ than it is for positive values. Like the average magnetic field, the centroid of the magnetic field also diverges as $\xi_w \to 2$ and the inner envelope approaches $r = 0$. This is true for all values of $(I_2-I_1)/I_b$ except $(I_2-I_1)/I_b = 1.0$.
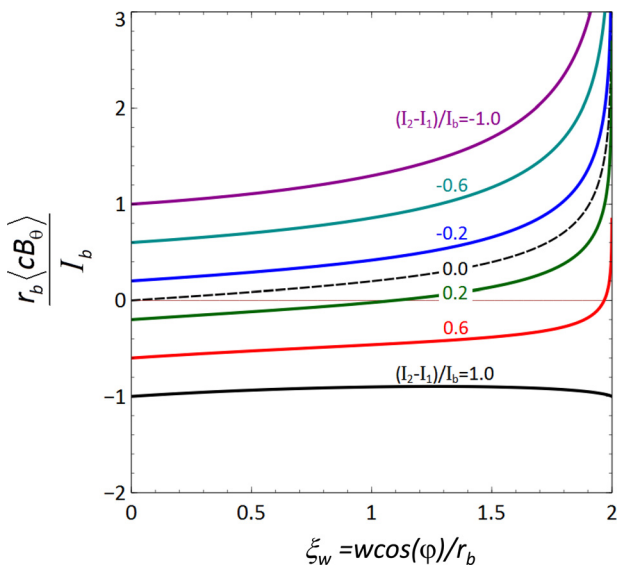

FIG. 2. The normalized average magnetic field as a function of the normalized beam width, ξ_w, for several values of $(I_2–I_1)/I_b$.
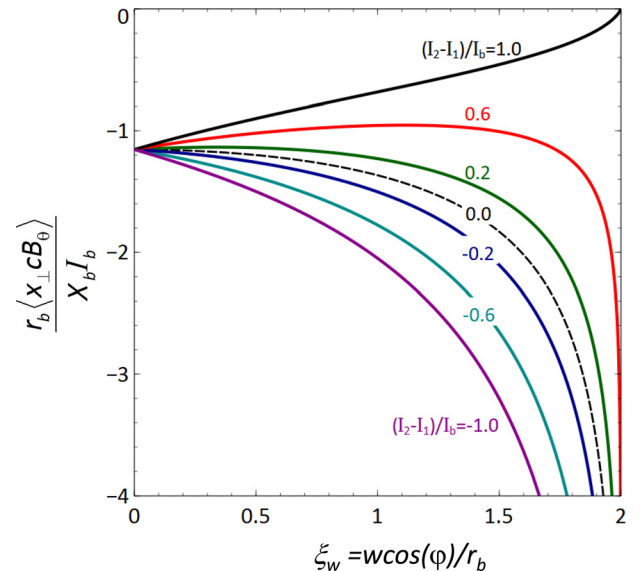
FIG. 3. The normalized centroid of the magnetic field as a function of the normalized beam width, ξ_w, for several values of $(I_2–I_1)/I_b$.

IV. SOLUTIONS TO THE ENVELOPE EQUATION FOR THE CURRENT DIVIDER

The simultaneous solution to the envelope equations (Eqs. (35) and (38)) with $\langle F_\perp \rangle$ and $\langle x_\perp F_\perp \rangle$ given by Eqs. (20) and (40) and appropriate initial conditions provides a solution for $r_0 = (r_b, z_b)$ and X_b. These equations collectively will be referred to as the envelope equations. The averages $\langle B_\theta \rangle$ and $\langle x_\perp B_\theta \rangle$ are given by Eqs. (44) and (45). In this section, several specific examples of the application of the envelope equations are presented.

The first example is a beam with a sufficiently large diameter such that the specific energy deposition on both the entrance foil and the target are below the threshold for plasma formation. In this case, the only source of transverse electric field reduction is from image charges on the entrance foil and target. For this example, a value of $f_i = 0.5$ is assumed to represent this field reduction. The beam parameters for this example are $I_b = 200$ kA, $(\gamma_0-1)mc^2 = 8$ MeV, and $\varepsilon = 200$ mrad-mm. The initial conditions at the entrance foil ($z = 0$) are: $r_b = 19$ cm, $w = 3$ cm, $\varphi = -20°$, and the initial slope of the envelope (dX_b/ds) is assumed to be zero. These values are rough estimates of the beam parameters at the end of the Mercury inductive-voltage adder[16] using a hollow cathode, indented anode diode.[6]

Envelope solutions with these beam parameters and initial condition are shown in Fig. 4 for four different values of (I_2-I_1). The black curves are the average trajectories of the beam and the red and blue curves are the beam envelope calculated as two standard deviations on either side of this orbit. Figure 4(a) also shows the initial size of the beam envelope ($\pm 2X_b$) at the entrance foil. As the beam propagates, there are oscillations in the envelope that evolve according to Eq. (38). These betatron oscillations are caused by an imbalance between the magnetic pressure and the beam's kinetic pressure.

Figure 4 further shows that the trajectory of the beam is controlled by the value of the difference of the two return currents (I_2-I_1). When (I_2-I_1) = 120 kA (Fig. 4(a)), there is a strong negative force on the beam which causes it to pinch inward toward the axis. When (I_2-I_1) = 40 kA (Fig. 4(b)), the net force on the beam is smaller and the beam trajectory is nearly straight. For (I_2-I_1) = -40 kA (Fig. 4(c)), the net force on the beam is now radially outward and the concavity of the average beam trajectory is now positive as it approaches $z = 20$ cm. For (I_2-I_1) = -120 kA (Fig. 4(d)), the slope of both the beam trajectory and envelope approaches $z = 20$ cm at nearly normal incidence. If a high-atomic-number (high-Z) target is located here, then the beam approaches the target at normal incidence. Because the radiation pattern is highly peaked in the direction of the electron trajectory, this is important for applications where bremsstrahlung production in the forward direction ($\varphi = 0$) is important. This beam condition can be obtained by choosing the inductances in the return-current path so that $I_1/I_2 = L_2/L_1 = 4$.

Another important application of an intense electron beam is that of a highly pinched, small-diameter beam. In this example, it is assumed that the beam diameter as it enters the current divider is smaller than that used in the last example but still large enough to avoid plasma formation on the entrance foil. However, at the target, it is assumed that the beam is so highly concentrated that plasma is formed there. Ions drawn from this plasma are attracted to the beam's space charge and flow in a direction opposite to the beam. The plasma density is assumed to be sufficiently large so that the positive space charge provided by this flow completely charge neutralizes the electron beam over its entire length. Therefore, $f_i = 1$ is used for this example. The beam parameters taken for the pinched-beam example are $I_b = 150$ kA, $(\gamma_0-1)mc^2 = 8$ MeV, and $\varepsilon = 200$ mrad-mm. The initial conditions at the entrance ($z = 0$) are: $r_b = 4.5$ cm, $w = 1$ cm, $\varphi = -20°$, and $dX_b/ds = 0$.

The envelope solutions for the pinched-beam example for four different values of (I_2-I_1) are shown in Fig. 5. Here, the envelope solution is stopped when the inner envelope crosses $r = 0$. When this occurs, the envelop solution diverges and the assumption of a hollow beam is no longer accurate.

It is interesting to note that both the amplitude and wavelength of the betatron oscillations get smaller as the
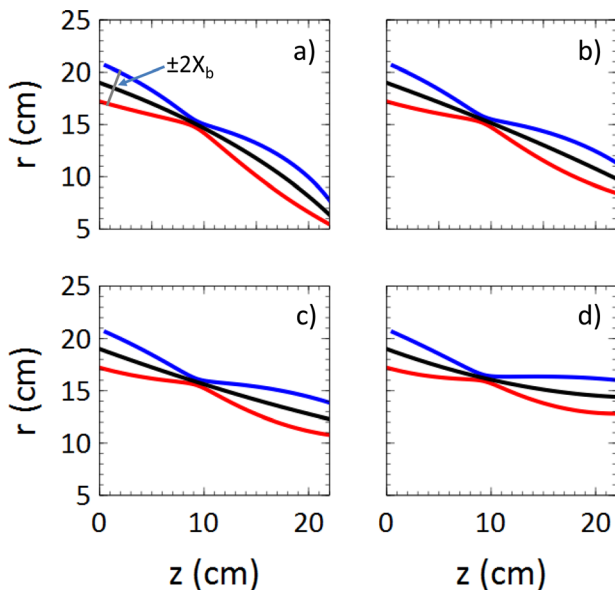

FIG. 4. Solutions to the beam-envelope equations for a large-diameter beam with $I_b = 200$ kA, $r_b = 19$ cm, $w = 3$ cm, $\varepsilon = 200$ mrad mm, and four different values of (I_2–I_1): (a) 120 kA, (b) 40.0, (c) -40 kA, and (d) -120 kA.
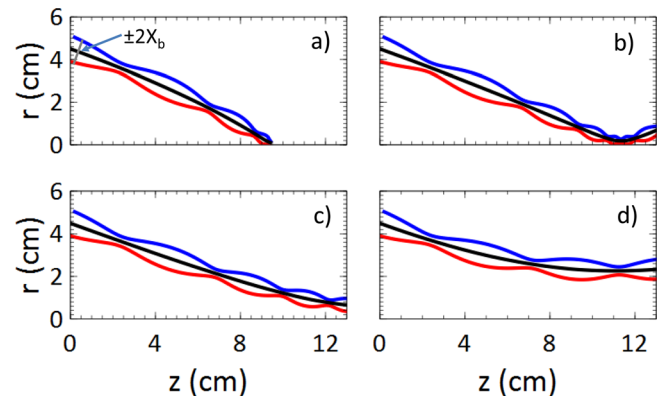

FIG. 5. Solutions to the beam-envelope equations for a small-diameter, pinched electron beam with $I_b = 150$ kA, $r_b = 4.5$ cm, $w = 1$ cm, $\varepsilon = 200$ mrad mm, and four different values of (I_2–I_1): (a) 20 kA, (b) 10 kA, (c) 0 kA, and (d) -20 kA.

beam approaches r = 0. This is the result of the spatially variation of the average magnetic field, which increases as $1/r_b$ (see Eq. (44)).

When $(I_2-I_1) = 20$ kA (Fig. 5(a)), the force on the beam is negative and the electron beam is pinched to a very small diameter. The width of the beam at the pinch location is about 1.2 mm. However, the average angle that the beam makes with the Z-axis is about $20°$. These beam parameters are interesting to flash x-radiography where a small x-ray spot and large dose in the forward direction are desirable.

Because the forward dose depends strongly on the beam angle, it is desirable to have the beam angle as close to zero as possible. As shown in Fig. 5(b), this can be achieved by reducing (I_2-I_1) to 10 kA. For this case, a tightly pinched beam is maintained with a width comparable to that in Fig. 5(a) and the average angle is close to $\varphi = 0°$ near z = 11 cm. Placing a high-Z target here produces both a small-diameter x-ray spot and maximizes the forward dose.

When $(I_2-I_1) = 0$ (see Fig. 5(c)), the force is now positive and the beam is no longer as tightly pinched. This shows that focusing a beam to a small diameter requires that the return current in the outer path (I_2) be slightly larger than the current in the return-current rod. This provides a negative magnetic field that helps confine the beam in a tight pinch as $r_b \rightarrow 0$. If a tight pinch is not as important as straightening the beam orbits, then this can be accomplished by decreasing (I_2-I_1) to -20 kA. As the beam approaches z = 12 cm, the average angle changes from $\varphi = -20°$ to $0°$ with an average beam radius of $r_b \approx 2$ cm.

V. CONCLUSION

This paper has presented a method for controlling the trajectory of a hollow electron beam using a passive current divider. In the current divider, the beam current is split between two return-current paths, which are determined by the return-current geometry. The average force on the beam is proportional to the difference between these two return currents, while the self-force on the beam envelope is proportional to the total beam current.

Solutions to the beam envelope equation for a hollow electron beam show that the beam properties at the target can be controlled by appropriate choice of the return-current-path inductances. Two different examples presented in the paper show that the beam properties can be manipulated to a wide range of final conditions. One of these desired conditions is the straightening of the beam so that the angles-of-incidence on a high-Z target are nearly normal. Another important example is the pinching of the beam to a small diameter. Appropriate choice of the return-current-path inductances shows that the current divider can produce a small-diameter beam with angles-of-incidence that are nearly normal on the target. For beam parameters that are consistent with those from the Mercury IVA (8 MV, 150 kA), the envelope solutions show that mm-size beams with angles approximately normal to the target are possible.

It should be cautioned, however, that the envelope equations are a quasi-equilibrium analysis that does not include possible non-stationary effects such as instabilities and

emittance growth. Also, as the dense plasma at the target thermally expands into the current divider, a region where the beam is both charge and current neutralized will likely be created. In this region, the confining force provided by the magnetic field is greatly reduced, which could cause the focal spot to move away from the target resulting in a larger than desired beam diameter at the target. These important effects require fully kinetic simulations and will be examined in a future paper. Proof-of-principle experiments are currently being planned and will also be reported in a future paper.

[1]S. B. Swanekamp, J. P. Apruzese, R. J. Commisso, D. Mosher, and J. W. Schumer, "An analysis of intense pulsed active detection (IPAD) for the detection of special nuclear materials," IEEE Trans. Nucl. Sci. **58**, 2047 (2011).

[2]J. Maenchen, G. Cooperstein, J. O'Malley, and I. Smith, "Advances in pulsed power-driven radiography systems," Proc. IEEE **92**, 1021 (2004).

[3]J. J. Ramirez, D. E. Hasti, J. P. Corley, J. W. Poukey, K. R. Prestwich, P. W. Spence, I. D. Smith, L. G. Schlitt, H. N. Nishimoto, and K. E. Nielsen, "The four stage helia experiment," in Proceedings of the 5th IEEE Pulsed Power Conference, Arlington, Virginia, 10–12 June 1985.

[4]A. A. Kim, B. M. Kovalchuk, A. N. Bastrikov, V. G. Durakov, S. N. Volkov, and V. A. Sinehryukhov, "100 ns current rise time LTD stage," in Proceedings of the 2001 IEEE Pulsed Power Plasma Sciences Conference, available online from IEEE Explore Document No. 0-7803-7120-8102.

[5]T. W. L. Sanford, J. W. Poukey, T. P. Wright, J. Bailey, C. E. Heath, R. Mock, P. W. Spence, J. Fockler, and H. Kishi, "Impedance of an annular cathode indented-anode electron diode terminating a coaxial magnetically insulated transmission line," J. Appl. Phys. **63**, 681 (1988).

[6]J. C. Zier, D. Mosher, R. J. Allen, R. J. Commisso, G. Cooperstein, D. D. Hinshelwood, S. L. Jackson, D. P. Murphy, P. F. Ottinger, A. S. Richardson, J. W. Schumer, S. B. Swanekamp, and B. V. Weber, "High-power, photofission-inducing bremsstrahlung source for intense pulsed active detection of fissile material," Phys. Rev. Spec. Top. – Accel. Beams **17**, 060401 (2014).

[7]T. W. L. Sanford, J. W. Poukey, J. A. Halbleib, and R. C. Mock, "Compound-lens injector for a pulsed 13-TW electron beam," J. Appl. Phys. **73**, 8607 (1993).

[8]R. B. Miller, *An Introduction to the Physics of Intense Charged Particle Beams* (Plenum Press, NY, 1982), pp. 85–87.

[9]E. P. Lee and R. K. Cooper, "General envelope equation for cylindrically-symmetric charged-particle beams," Part. Accel. **7**, 83 (1976).

[10]R. J. Adler, "Image-field focusing of intense ultra-relativistic electron beams in vacuum," Part. Accel. **12**, 39 (1982).

[11]S. Humphries, "Equilibria for foil-focused relativistic electron beams," Part. Accel. **13**, 249 (1983).

[12]A. E. Blaugrund, G. Cooperstein, and S. A. Goldstein, "Relativisitic electron beam pinch formation processes in low impedance diodes," Phys. Fluids **20**, 1185 (1977).

[13]P. Tchebichef, "Des valeurs moyennes," J. Math. Pures Appl. **12**, 177–184 (1867).

[14]P. L. Meyer, *An Introduction to Probability and Statistics*, 2nd ed. (Addison-Wesley Publishing Co., Reading, MA, 1970), pp. 141–142.

[15]R. C. Davidson, H. Qin, S. I. Tzenov, and E. A. Startsev, "Kinetic description of intense beam propagation through a periodic focusing field for uniform phase-space density," Phys. Rev. Spec. Top. – Accel. Beams **5**, 084402-1 (2002).

[16]R. J. Allen, R. J. Commisso, G. Cooperstein, P. F. Ottinger, and J. W. Schumer, "Extension of the operation point of the Mercury IVA from 6 to 8 MV," in Proceedings of the 2011 IEEE Pulsed Power Conference, available online from IEEE Explore Document No. 978-1-4577-0631-8/12.